



Research Article

GEOLOGY

Integrating Remote Sensing and Aeromagnetic Data to Delineate the Structural Elements and Mineralization Zones in Safaga Area, Eastern Desert, Egypt

Hamed A. Alrefaee¹, Samir Z. Kamh^{2*}, Mohamed M. Elhossainy¹

¹Geology Department, Faculty of Science, Kafr Elsheikh University, Egypt

²Geology Department, Faculty of Science, Tanta University, Tanta 31527, Egypt

*Corresponding author: Samir Kamh

e-mail: skamh@science.tanta.edu.eg

Received: 2/7/2023

Accepted: 16/7/ 2023

KEY WORDS

aeromagnetic
remote Sensing
structural elements
mineralization
Safaga

ABSTRACT

Mapping the structural lineaments and associated mineralization zones represents an essential step for exploration and extracting new mineral resources required for industrial purposes and economic growth. The present study integrates available remote sensing and aeromagnetic data for Safaga area to deduce the structural lineaments and possible associated mineralization, that represent promising economical zones for mineral exploration. The remote sensing data including Landsat-8 and Sentinel-2 were used to produce an update geologic map and mineralized zones of the study area. The radar data of Sentinel-1 was used to extract the surface structural lineaments that were found striking NW-SE, NNW-SSE, N-S and NE-SW. Residual magnetic anomalies, on the other hand, helped in locating the subsurface causative bodies where the edge detection method clearly outlined the edges of these subsurface magnetic sources. Moreover, the magnetic Euler deconvolution and structural complexity determined trends and depths of subsurface structural lineaments. The structural lineaments delineated by the remote sensing techniques quite match those delineated by the magnetic data analysis. The integration between the remote sensing and aeromagnetic data can therefore be helpful in determining promising mineralization zones.

Introduction

The two optical sensors of the Landsat-8 OLI/TIRS and Sentinel-2 data have an effective contribution in identifying the lithological rock varieties, mineralization zones and structural elements (Zoheir *et al.*, 2019; Abd El-Wahed *et al.*, 2021). The specific spectral features of hydroxyl, iron oxides, carbonate, clay, and sulfate minerals in visible, near-infrared, and short-wave infrared regions can be utilized to determine zones of hydrothermal alteration and their associated mineralization (Hunt, 1977). Their absorption and reflection signatures in the visible near-infrared region (0.4 - 1.1 μm) are affected by the presence of Fe^{2+} , Fe^{3+} , Cr, Mn, Ni, and Co elements in these minerals. The OH-bearing minerals have definite absorption signatures in the short-wave infrared region (SWIR) (2.0 to 2.50 μm) which can be detected also by the Landsat-8 and Sentinel 2 data (Clark *et al.*, 1990). On the other hand, the radar data of Sentinel-1 is a powerful tool to detect the structural elements and regimes. The longer wave lengths of (L-band) of radar data can penetrate the ground surface to provide useful information about the structural elements (Kusky and Ramadan, 2002). Pour *et al.*, (2018) used Sentinel-1 L-band to extract the structural lineaments and

their associated mineralization in arid and semi-arid regions.

The magnetic anomaly originated due to an anomalous signature produced by magnetite-rich zones that are clearly distinguishable from the host rocks. Magnetic data are cost-effective, cover wide areas, and have several applications in exploration. They are used as an effective technique for mapping regional structures and lithology (Kadasi, 2015) and are commonly used for mineral prospecting everywhere in the world (Murphy, 2007), particularly for mapping the structural features and detecting the physical properties of rocks (Telford *et al.*, 1990; Xiong *et al.*, 2014). The aeromagnetic data are commonly and effectively used to identify the subsurface structural elements based on the geomagnetic field variations resulting from the unequal distributions of the magnetite content within the hosted rocks. Such structural elements represent conduits for minerals accumulation associated with hydrothermal solutions. They are also used in automated mapping of porphyry gold/copper deposits and highly-concentrated zones of sulfide deposits. The structural mapping aids in delineating the structurally-controlled regions of ores mineralization. In areas

of exposed basement rocks on the surface, the magnetic anomaly reflects the amount of the magnetic content of the rocks (**Alexander et al., 2015**). Variations in the magnetic signatures associated with fault zones and fractured areas mark/indicate favorable locations of mineralization.

Several researchers conducted geological and geophysical studies on sparse regions within the Egyptian Eastern Desert. **Gabr et al., (2010)** conducted remote Sensing study to extract and locate alteration zones and associated gold deposits in Abu Marawat area, NED, Egypt. **Khamis and Ayoub (2014)** adapted integration of multidiscipline datasets, including aeromagnetic, ground and airborne radiometry, remote sensing, and geological data to characterize factors affecting the distribution of radioactive elements within Al Aglab area, NED, Egypt. **El-Magd et al., (2015)** utilized the ASTER images to delineate the structural pattern, map lithology, and detect alteration zones responsible for gold mineralization in the Fawakhir region. **Gaafar, (2016)** utilized aeromagnetic survey to outline preferable structural accumulations for gold mineralization's within Wadi of Yoider, Southern Eastern Desert. He included that gold mineralization and

hydrothermal alteration zones are mainly controlled and influenced by ENE-WSW faults. **Zaki et al., (2017)** used the aeromagnetic dataset for constructing a subsurface structural map and determining the depth to the basements in Gasus area, CED, Egypt. **Ahmed (2018)** integrated satellite images and airborne magnetic data to map the boundaries of the lithological rock units and reveal the structural setting affecting the radioactive minerals distribution in west Safaga region. **Abdelkareem et al., (2018a)** predicted mineral deposits associated with zones of hydrothermal alteration in the CED through integrating magnetic and remote sensing datasets. **Abdelkareem et al., (2018b)** integrated magnetic, geochemical, and satellite imagery to detect target potential zones for minerals exploration and produce minerals prospect map. **Elkhateeb and Abdelatif (2018)** utilized aeromagnetic and airborne radiometric data to map lithologies and delineate both the structural features and zones of hydrothermal alteration to locate gold mineralization accumulations. **Eldosouky et al., (2020)** highlighted gold mineralization associated with zone of hydrothermal alteration in Allaqi-Heiani Suture zone, SED, Egypt using aeromagnetic data and Landsat images.

The key objective of this study is determining optimal areas of mineralization and hydrothermal zones based on identification of surface and subsurface structures through integration of aeromagnetic data and remote sensing images. This will also help in recognizing the different lithologic units and highlight the possible zones of mineralization. A predictive map of mineral deposit zones will be constructed and validated by field observations/investigations and metallogenic data.

Study area

The studied area occupies a vast district within Egyptian Eastern Desert (ED), where the major part is located in Central Eastern Desert (CED) and a minor portion in Northern Eastern Desert (NED) (**Fig. 1**). The area is bounded by longitudes $33^{\circ} 30'$ to $34^{\circ} 05'$ E and latitudes $26^{\circ}15'$ to $26^{\circ}45'$ N, covering nearly 2898 km^2 . It is primarily covered by basement exposures which consist of moderately high and rough mountains that have several protuberant summits, their elevations reach up to 1016 m. The area is dissected by many wadis such as Wadi (W.) Um Taghir el-Foqani, W. Safaga, W. Gasus and W. Quei (**Fig. 1**).

The area is occupied by a complex variety of serpentines and ophiolitic metagabbros that constitute the

ophiolitic mélange. The metagabbrodiorite and metavolcanics cover vast area. The Dokhan volcanics (non-metamorphic volcanic rocks that range in their composition from acidic to intermediate) and Hammamat clastics (clastic sediments with molasse facies) are distributed in the eastern part of the area. Moreover, older and younger granites range in their compositions between granodiorite and alkali-feldspar granite (**Fig. 1**). In addition to the basement rocks the area comprises Phanerozoic rock units and Quaternary sediments.

Geological and structural setting

The Eastern Desert is subdivided to three terranes according to the variations of the lithology and tectonic setting (**Stern and Hedge, 1985**). It is divided by two main structural discontinuities into three distinguished lithotectonic provinces; North (NED), Central (CED), and South (SED). Fowler et al. (2006) stated that Barud Shear zone splits the NED from the CED, while CED is separated from the SED by the Shear zone of Shai't-Nugrus (**Fowler and Osman, 2009**). The NED is dominated by a plenty of granite plutons (syn-tectonic granites) with a variety of gneisses, existence of Dokhan volcanics type locality, less abundant of Hammamat sediments, and one of the

greatest dike swarms in the entire world (Windley, 1996).

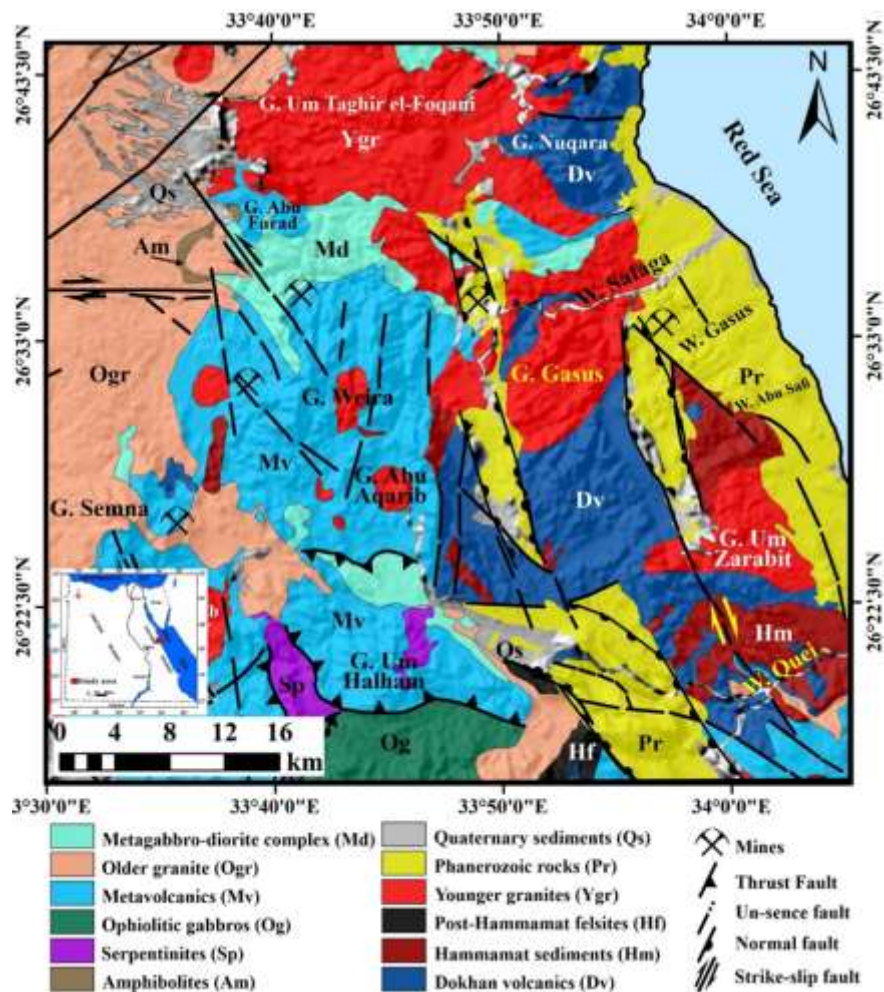


Fig. (1): The geologic map of the study area (modified after Egyptian Geological Survey and Mining Authority, 1992).

The NED is distinguished by lack of ophiolitic ultramafic, pillowed basalts, and NW shear zones, which abundantly exist in CED (El Gaby *et al.*, 1988). Beside the previous rock units that exist in NED, CED is marked by the presence of reasonable exposures of the ultramafic rocks, significant portions of the ophiolitic sequence and mélanges, and larger amounts of volcanogenic sediments and arc-type volcanics (Sims and James, 1984). The Hammamat

sediments have widespread exposures and their type locality (Wadi El Hammamat) marked in the CED. The Hammamat sediments were mainly deposited in inter-mountain basin, demonstrating unstable tectonic setting (Grothaus *et al.*, 1979) or rifted basin (Greiling *et al.*, 1994). Great strike-slip faults with left lateral movements comparable to Najd-fault of Arabian Shield exist in the CED province (Stern *et al.*, 1984). The SED is characterized

by the existence of the pre- Pan-African rocks of the medium-grade gneiss, which include continental shelf sediments intruded with alkali granitoids. These rocks are exposed underneath ophiolitic belt that is encompassed between the NW–SE trending orogenic belts (O'Conner *et al.*, 1993). The SED domain is dominated by the ENE to NE dike swarms; however, the NW swarms are present too.

The geological structures within the study region are mainly represented by fractures, faults, and shear zones. These structural features include NW–SE (Red Sea or Suez Gulf) trending thrust faults and NE-SW (Gulf of Aqaba) fractures. ENE–WSW and NNW–SSE trending fractures and normal faults are also present (Stern, 1985). According to Habib (1987), three tectonic movements affected the study area; the Meatiqian orogeny dominated Nile craton (Gass, 1977), the Abu Ziran event resulted in NW - SE compressional trend, and the Abu Diwan movement formed NNW – SSE directed fractures. The structural features with E-W and N - S trends are less common.

Data and methodology

Satellite datasets and pre-processing

Lithological mapping for the investigated area is based principally on the Landsat-8 and Sentinel-2 data. They

are used in discriminating different rock-units of serpentinites, ophiolitic metagabbros, metavolcanics, metagabbro-diorite, granitic rocks, Hammamat sediments and Dokhan volcanics in the study area. The applications of the band math algorithms on the two datasets help in locating the mineralized zones in the area. Landsat-8 OLI sensor exhibits VNIR and SWIR spectral bands (1–7 and 9), which have a 30-m spatial resolution, while band 8 as a panchromatic has a 15-m resolution. Bands (2-7) are effective in mineralogical and geological maps. The SWIR and VNIR spectral bands of Sentinel-2 are represented in the bands (2, 3, 4, and 8) with a 10-m resolution, whereas bands (5, 6, 7, 8A, 11 and 12) have a 20-m resolution.

Two cloud-free Landsat-8 and Sentinel-2 images have been layer-stacked and subsetting, then processed using ENVI 5.3 software. They have been corrected to the UTM projection (Zone N36) according to WGS-84 datum. Landsat-8 bands have been resampled to 10 m of the Sentinel-2 using pan sharpening to improve small areas of mineralization's zones. Radiometric and atmospheric correction have been applied to the two datasets. Fast Line of Sight Atmospheric Analysis of Hypercubes (FLAASH) algorithm has been used to

eliminate the effects of atmosphere in the Landsat-8 image, whereas the Sentinel-2 data have been corrected utilizing the software of Sentinel Application Platform.

Several image processing techniques including band combination (BC), band ratios (BR), Minimum Noise Fraction (MNF), Principal Component Analysis (PCA), and Decorrelation Stretch (DS) have been applied to enhance lithological contacts, structural elements and their associated mineralization features. Band combination has been presented in the RGB mode depending on the spectral properties of the employed data. The band ratios (BR) are simple and effective process to enhance the accurate lithological discrimination. The used data can be reduced and presented in the highest data variation in first principal component by using (PCA) algorithm. The (MNF) approach can also rotate the two satellite datasets in an orthogonal tends to provide helpful principal components. Decorrelation stretching (DS) is considered as a direct and simple technique that allows correlation among the used spectral bands and enhances the lithological contacts.

As the structural elements have principal role in accumulating and controlling mineralization zones. Therefore, regional

structural features of the main faults, thrusts, and strike slip faults were first detected from the processed Sentinel-2 and Landsat-8 images depending on the tonal variations and visual inspection. These structural elements were then verified through field investigations. The structural lineaments /fractures were extracted from Sentinel-1 data automatically using PCI Geomatica software. The Sentinel-1 dataset is improved using Lee adaptive filtering to resolve lineaments, edges, and structural elements. The (VH, VV, and VV+VH) bands have been processed using PCA algorithm to extract the most informative component of PC1. The LINE extraction module in PCI Geomatica was applied to PC1 image to extract the linear structural features and lineaments. The extracted lineaments map is imported in Rockwork software for generating azimuth-frequency diagram and defines the most dominant structural tends in the study area. The extracted structural features and mineralized zones are integrated and correlated with that extracted from the aeromagnetic data.

Geophysical data

Magnetic data

The total magnetic intensity (TMI) map that is extracted from the airborne magnetic survey acquired by the Aero-Service Division of Western

Geophysical Company (Aero Service Company, 1984) represents the available geophysical data for the current study. The data are acquired for Egyptian Geological Survey and Mining Authority (EGSMA) and Egyptian General Petroleum Corporation (EGPC). Airborne magnetic survey was conducted at parallel NE-SW flighting lines with 1500 m intervals and the tying lines in NW–SE direction with lines spacing 10 km. The survey was acquired at elevation of 120 m and with station interval of 50 m.

Reduction to the pole (RTP) map

Baranov (1957) presented the “reduction to the pole” mathematical procedure to transform total magnetic data measured at any location to magnetic anomaly as it was collected at north pole to eliminate the magnetic anomaly’s bipolarity nature. The total magnetic intensity underwent is processed to the International Geomagnetic Reference Field, then gridded and reduced to the RTP magnetic grid.

Residual magnetic anomalies map

In the current study, a Gaussian filter with 0.015 (Radian/km) cutoff wave-number is applied to the RTP magnetic map to separate the residual magnetic component from the regional one. The Gaussian filter was chosen to separate the regional and residual

components since it perfectly separates the lowermost effect from the ambient noise (Ismail, 2008). Residual magnetic component maps illustrate and enhance the residual anomalies associated with the local near-surface magnetic source bodies (**Blakely, 1996; Lowrie, 2007**).

Edge detection

Geophysical magnetic interpretation aims to the precise detection of horizontal edges and boundaries of subsurface sources and structures. Magnetic prospecting and drilling for mineral accumulations are influenced and optimized by accurate resolving of the magnetic body’s geometry. Edge detection aids in outlining lateral extents of the magnetic source bodies (**Nabighian et al., 2005**).

The edge detectors are commonly used for several geophysical prospecting purposes, including mapping faults, dykes, geological contacts, and identification of ore accumulations (**Oruc, 2011**). The horizontal tilt derivative (abbreviated to TDX) filter was recently presented as a detector of edges by Cooper and Cowan (2006). The TDX shows maximum magnetic value above the magnetized body edges and distinguishes the body edges better than the tilt angle. The TDX is given by the following mathematical expression:

$$TDX = \text{atan} \frac{\sqrt{\left(\frac{\partial F}{\partial x}\right)^2 + \left(\frac{\partial F}{\partial y}\right)^2}}{\left(\frac{\partial F}{\partial z}\right)}$$

Euler deconvolution

Reid *et al.*, (1990) introduced Euler's method to locate the magnetic sources automatically and computed their depths. Euler's homogeneity of Thompson (1982) is given by the following formula:

$$(x - x_0)(dM/dx) + (y - y_0)(dM/dy) + (z - z_0)(dM/dz) = N(B - M)$$

Where x_0 , y_0 , and z_0 refer to the subsurface magnetic source's location. M refers to the magnetic field at the (x, y) location. B refers to the regional magnetic field and N refers to the structural index.

Structural complexity

The center of exploration targeting (CET) method enhances the magnetic texture to enable mapping the structural complexity (SC) regions for exploration processes. The (SC) aids to identify the promising zones for ore deposits. The technique employs a detector that is based on two-sided symmetric point to examine the texture for detecting discontinuities in the magnetic dataset (Kovesi, 1991; Holden *et al.*, 2010). The CET includes a set of mathematical procedures and algorithms, which aid detection and enhancement of lineament

and delineation (SC) of the potential field dataset (Holden *et al.*, 2008).

Results and Discussion

Lithological discrimination and mineralization zones detection

The Landsat-8 and Sentinel-2 datasets were processed by numerous digital images processing algorithms to enhance lithological contacts, highlight mineralized zones and structural elements. The band combination 753 in RGB of Landsat-8 highlighted the basic rocks of Dokhan volcanics in dark green pixels, the metavolcanics in dark brown and the granitic rocks appeared in light brown pixels (Fig. 2a). The band ratio (7/5, 5/4, 6/7) in the RGB of the Landsat-8 provided fantastic lithological discrimination. It presents the serpentine in magenta color, the metavolcanics in bloody red color, the Dokhan volcanics and Hammamat sediments exhibit non-homogeneous pixels of variegated colors dominated with dark green and the granitic rocks appear in yellowish green color (Fig. 2b). The Phanerozoic rocks displayed cyan pixels color. NW strike-slip faults are easily noticed due to tonal variations of the rock units (Fig. 2b). Band ratio (11/12, 4/2, 4/11) of Sentinel-2 was utilized to detect the intercalation between Dokhan volcanics and Hammamat sediments with bright violet and orange pixels, respectively (Fig. 2c). The island metavolcanics are exhibiting

dark blue color while the granitic rocks were detected by bright green pixels (**Fig. 2c**). The PCA-321 in RGB components of Sentinel-2 gives excellent lithological differentiation of metavolcanic rocks as bluish magenta, Dokhan volcanics and Hammamat sediments as reddish beige and granitic rocks as greenish violet (**Fig. 2d**). The NNW-elongated exposures of Phanerozoic rocks exhibit fantastic red color (**Fig. 2d**). The MNF-321 in the RGB of Sentinel-2 shows outstanding distinction of metavolcanics as dark magenta, Dokhan volcanics and Hammamat sediments have cyan color pixels (**Fig. 3e**). The decorrelation stretching DS-652 in the RGB of Landsat-8 outlined metavolcanics in bright violet dissected by dark green pixels of metagabbros. A unique separation of the Hammamat sediments and Dokhan volcanics in dark to bright green pixels could be obtained (**Fig. 2f**). The discriminated rock units are presented in **Fig. (1)** as an updated geological map of study area, which is verified by previous geologic maps and field work.

To detect the mineralized zones which are mostly rich with alteration minerals, band ratios of specific bands of Landsat-8 and Sentinel-2 were adopted

to enhance the pixels exhibit those minerals. The produced band ratios were presented as gray-scale mode that is thresholded to extract pixels representing the target minerals/alteration zones. The delineated pixels which are rich with minerals/alteration zones are overlaid on their images with a specific color to locate the spatial distribution of alteration zones within the research area (**Fig. 3a-e**). Iron oxide/hydroxides minerals are detected by the band ratio 4/2 of Landsat-8 that is superimposed with yellow color (**Fig. 3a**). The argillic alteration zones (e.g. kaolinite, montmorillonite, illite) were detected by the band ratio 6/7 of the Landsat-8 that is superimposed by red color (**Fig. 3b**). The propylitic alteration zones (e.g. epidote, chlorite, carbonate) were identified by the band ratio of 11/12 of Sentinel-2 and demarcated by cyan color (**Fig. 3c**). The gossan was also detected by the band ratio 4/11 of Sentinel-2 and located by the violet color (**Fig. 3d**). The detected alteration and mineralization zones in the study area are presented in a shaded relief map (**Fig. 3e**). These mineralization zones are associated with the basement rocks of serpentinite, metavolcanics, Dokhan volcanics and granitic rocks.

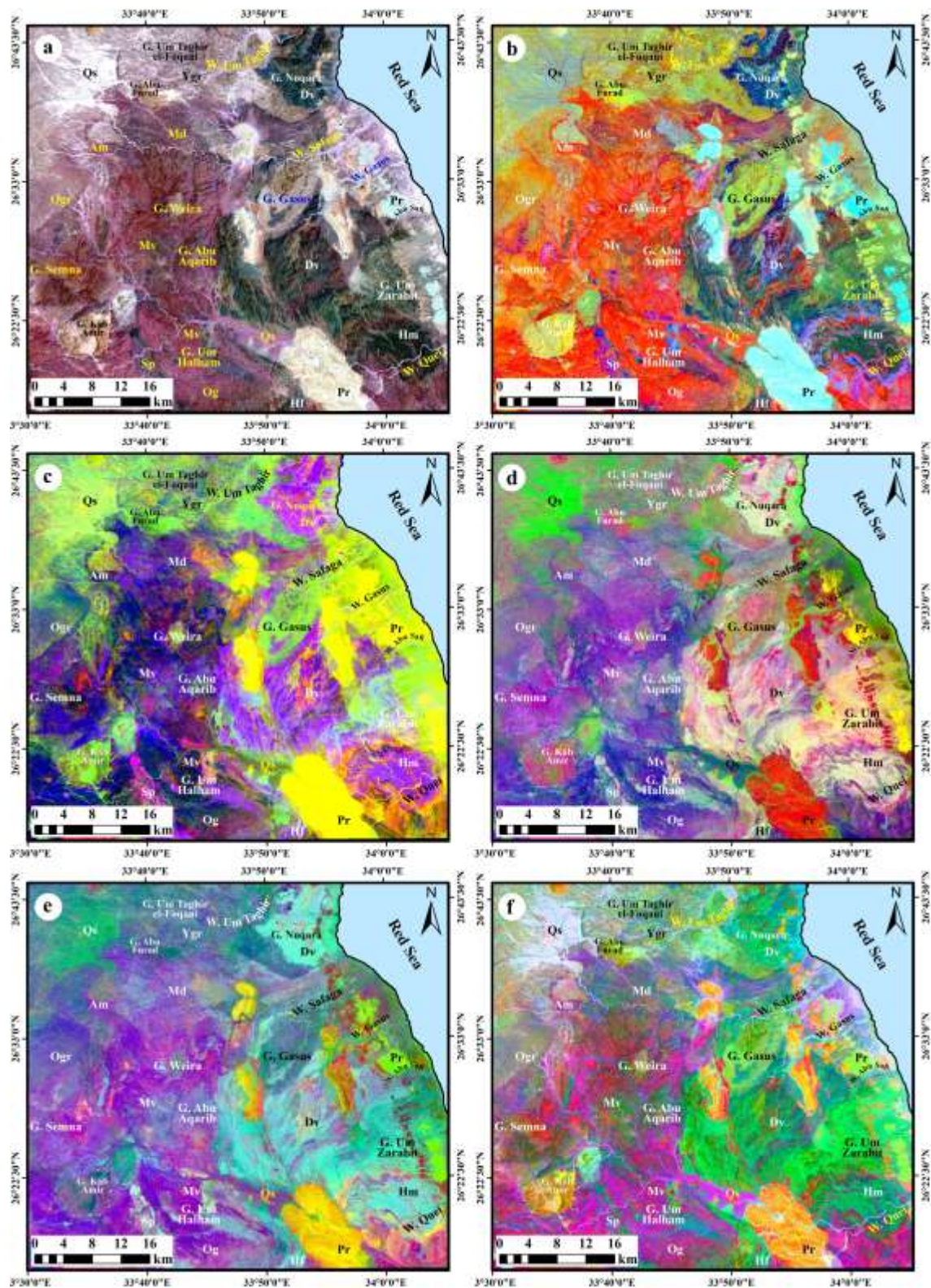


Fig. (2): Lithological discrimination via (a) Band combination RGB-753 of Landsat-8, (b) The band ratio of 7/5, 5/4, 6/7 in RGB of Landsat-8, (c) The band ratio of 11/12, 4/2, 4/11 in RGB of Sentinel-2, (d) PCA-321 of Sentinel-2, (e) MNF-321 in RGB of Sentinel-2 and (f) The decorrelation stretching DS-652 in RGB of Landsat-8. For Abbreviations see Fig. (1)

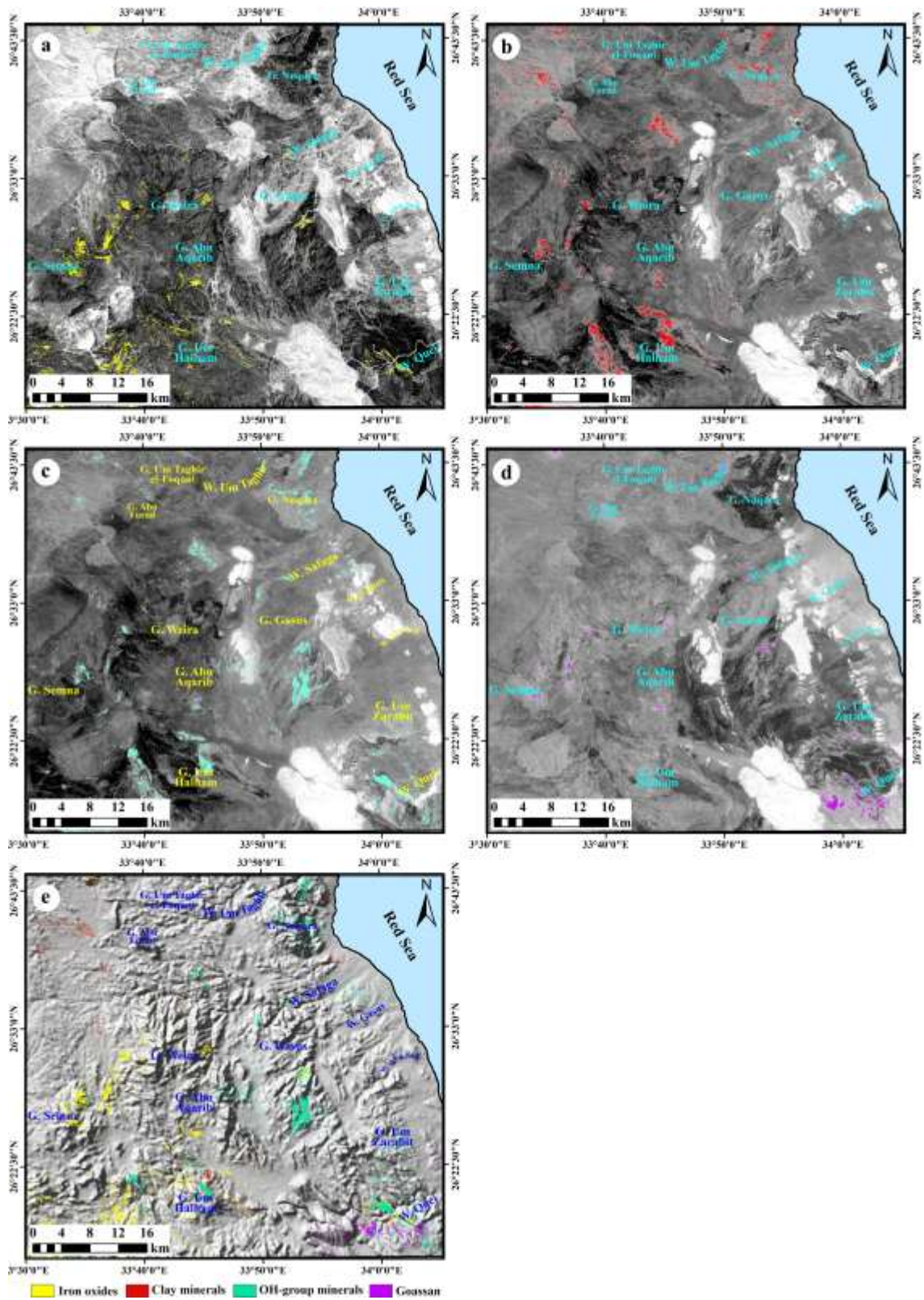


Fig. (3): Mineralization zones detection of iron oxides by band ratio of 4/2 of Landsat-8 (yellow pixels) (a), Clay minerals by band ratio of 6/7 of Landsat-8 (red pixels) (b), Hydroxyl-bearing minerals by band ratio of 11/12 of Sentinel-2 (cyan pixels) (c), Gossan by band ratio of 4/11 of Sentinel-2 (violet pixels) (d) and (e) grouping of all the mineralization zones in the study area.

Geophysical data

Reduction to the pole (RTP)

The RTP map displays a large number of magnetic zones with various polarities that trend in the N-S, NNW-SSE, and NNE-SSW directions (**Fig. 4a**). These appearances are basically due to variation in the basement relief and the susceptibility contrast within the basement complex. The map displays numerous closed anomalies, which have different shapes, trends, and amplitudes. The high (positive) magnetic anomalies exist in the northern, eastern, and southwestern parts and trend in N-S with amplitudes (60 to 1015) nano Tesla. The positive anomalies seem to be subdivided into many smaller positive anomalies. On the other side, low (negative) magnetic anomalies occupy western, central, northeastern, southeastern, and southern parts with shapes ranging from semicircular to ovoidal and elongated features. The negative anomalies have amplitudes that range from about -90 to -1040 nano Tesla.

Residual magnetic anomalies

The residual magnetic map displays several small semicircular and elongated magnetic anomaly closures (**Fig. 4b**). The map displays alternative positive and negative local anomalies, trending mainly in the N-S direction.

The map also displays few local anomalies directed in NNW-SSE and NNE-SSW. The positive and negative magnetic anomalies have been enhanced, defined, and increased in number. The amplitudes of the positive anomalies range from about 20 to 480 nano Tesla, whereas the amplitudes of the negative anomalies range from -30 to -430 nano Tesla. It seems that the positive anomalies coincide with mafic and ultramafic rock exposures including gabbro, metagabbro, and serpentinites, while the negative anomalies coincide with granites, metasediments, and Hammamat sediments.

Edge detection

The horizontal tilt derivative (TDX) map illustrates magnetic maxima above edges (**Fig. 4c**). The TDX map shows clearer and sharper edges compared to those shown by tilt derivative. The map confirms that the majority of the causative bodies are mainly arranged in the N-S trend with minority in the NW and NE trends.

The Euler map shows grouping of magnetic solutions primarily in N-S, NNW-SSE, and NNE-SSW directions (**Fig. 4d**). There are minor clusters in NW-SE, NE-SW, and E-W trends. The magnetic solutions exist at depths ranging from the ground surfaces to 490 m.

Lineaments extraction and structural complexity

Sentinel-1-based lineaments extraction

Generally, the mineralized zones in the Egyptian Eastern Desert exist close to or within the fracture systems. Lineaments and/or fractures systems contribute effectively to the hydrothermal fluids transmission to form the ore deposits. In the present study, the principal component PC1 of Sentinel-1 was used to extract the lineaments,

where this component contains the most important information. The extracted lineaments map shows that linear features dissected all rock units with different densities (Fig. 5a). It offers high density and linear intersection over the basement rocks. The metavolcanics, Dokhan volcanics, Hammamat sediments and granite exhibit large number of lineaments with high density (Fig. 5b).

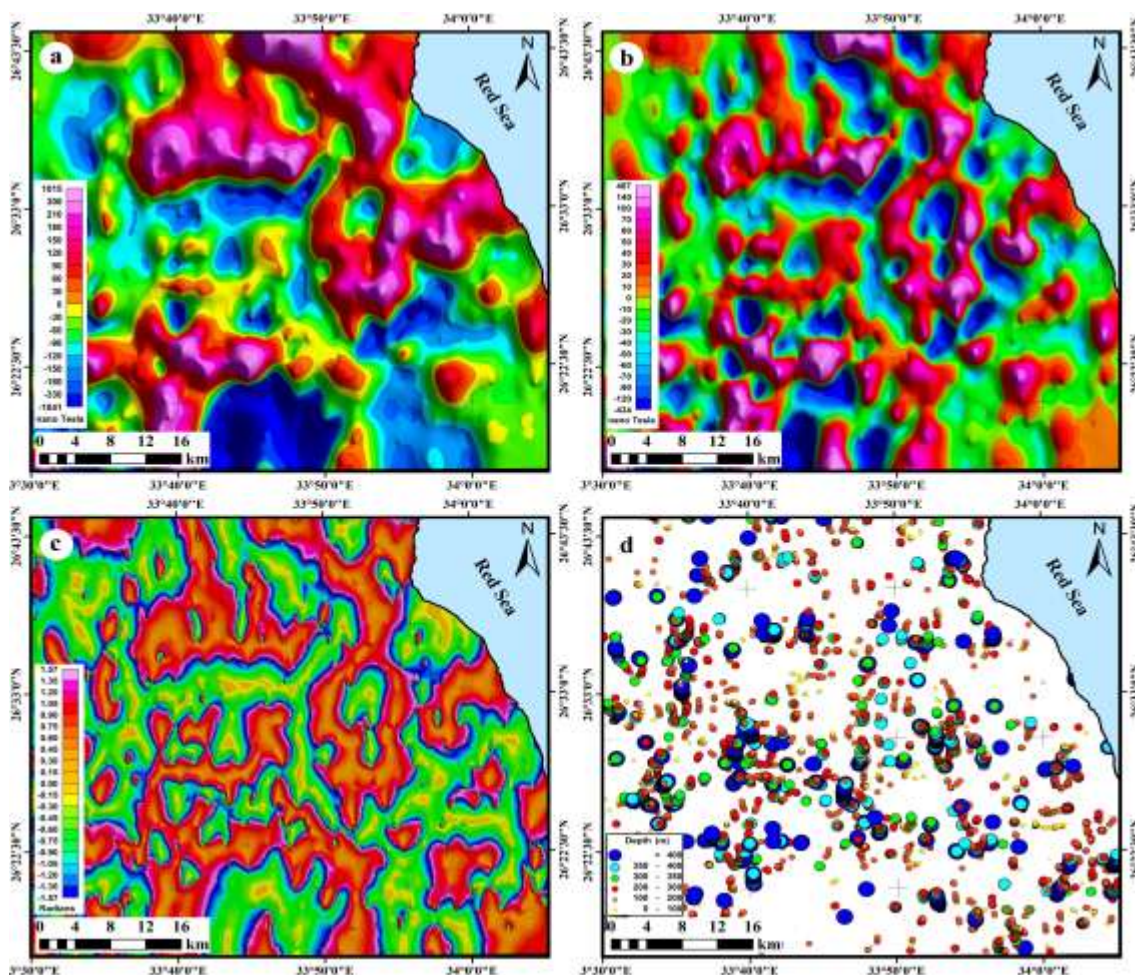


Fig. (4): (a) The RTP map of the study area showing the high magnetic values in magenta and red colors, whereas the low magnetic values are shown in blue color, (b) The residual magnetic map showing several local high magnetic anomalies mainly arranged in N-S direction. The local low magnetic anomalies are also mainly arranged in N-S direction, (c) The magnetic horizontal tilt derivative map displaying sharper and better edges of the positive magnetic causative sources and (d) The map of the magnetic Euler solutions using structural index (SI= 1).

The number of extracted lineaments is about 8619 features with an entire length of 5125.83 km. Their lengths range between 0.003 and 4.26 km with an average of 0.595 km. The azimuth frequency diagram (rose) displays the predominant linear structures as NW-SE, NNW-SSE, N-S, and NE-SW trends in decreasing order (**Fig. 5a**).

Geophysical data-based lineaments extraction

The linear structures were identified and extracted from the magnetic data using the CET method. The approach was achieved through successive procedures, including estimating the magnetic variations using the standard deviation, separating continuous lines using the phase symmetry, and enhancing the lineaments using amplitude threshold to suppress background signals and noise. These linear structures are shown by the vectorization map (**Fig. 5c**). The map displays the lineaments dominating the basement rocks, which look deformed by several structural trends. The estimated number of the determined lineaments is 308 segments having a total length of 554.48 km. Their lengths range between 0.036 and 6.16 km with an average of 1.8 km. The lineaments density map shows high densities over the basement

rocks (**Fig. 5d**). The azimuth frequency diagram (rose) displays predominant lineaments trends toward N-S, NNW-SSE, NW-SE and NE-SW in decreasing order. The two diagrams of azimuth frequency reflect a good comparison in the predominant linear structure's directions extracted from both the remotely sensed and geophysical data.

Figure (5e) shows the vectorization (structural complexity) map superimposed on the horizontal tilt derivative map. The lineaments of the structural complexity map match with the edges of the causative source bodies. This matching strongly indicates that lineaments, which are recommended zones for ore accumulations coincide with the edges of the subsurface magnetic sources.

Relation of mineralization to structural elements

The dominated trends of the extracted lineaments of the NW-SE, N-S, NNW-SSE and NE-SW coincide greatly with large-scale fractures and strike-slip faults (**Fig. 5f**). The detected mineralized zones were superimposed on the lineaments density maps. Figure (5f) shows that the highest lineament density is associated with mineralization. The geographic distribution of mineralized zones and lineaments density are highly matched revealing the role of lineaments

in the mineralization accumulation processes and that ore deposits formation was greatly controlled by the structural systems. The presence of the mineralization zone was verified with location of the old mines which appeared in **Fig. (5f)**.

Conclusion

The present study integrated remote sensing and geophysical data for mapping lithologies, extracting structural elements, and identifying mineralization zones within the Safaga area. Therefore, two optical sensors of Landsat-8 and Sentinel-2 were used to produce an updated geologic map and locate the mineralization zones. Different image processing procedures, such as band ratioing (BR), band combinations (FCC), Minimum Noise Fraction (MNF), Principal Component Analysis (PCA), and Decorrelation stretching (DS) were applied. Radar data of Sentinel-1 was

used to extract the lineaments map, which showed good correlation with spatial distribution of mineralized zones. The aeromagnetic data was transformed to the RTP map, which was subjected to many analyzing techniques such as regional-residual separation, edge detection, Euler's method, and structural complexity with the purpose of delineating the subsurface lineaments and their predominant directions as well as determining mineralization zones. The results obtained from the analysis of magnetic data reveals a good correlation with those obtained from the remote sensing data analysis. The extracted lineaments from the two dataset sources recorded NW-SE, NNW-SSE, N-S and NE-SW directions. These lineaments and the major structural elements have a great effect in the spatial distribution of the mineralization zones in the study area.

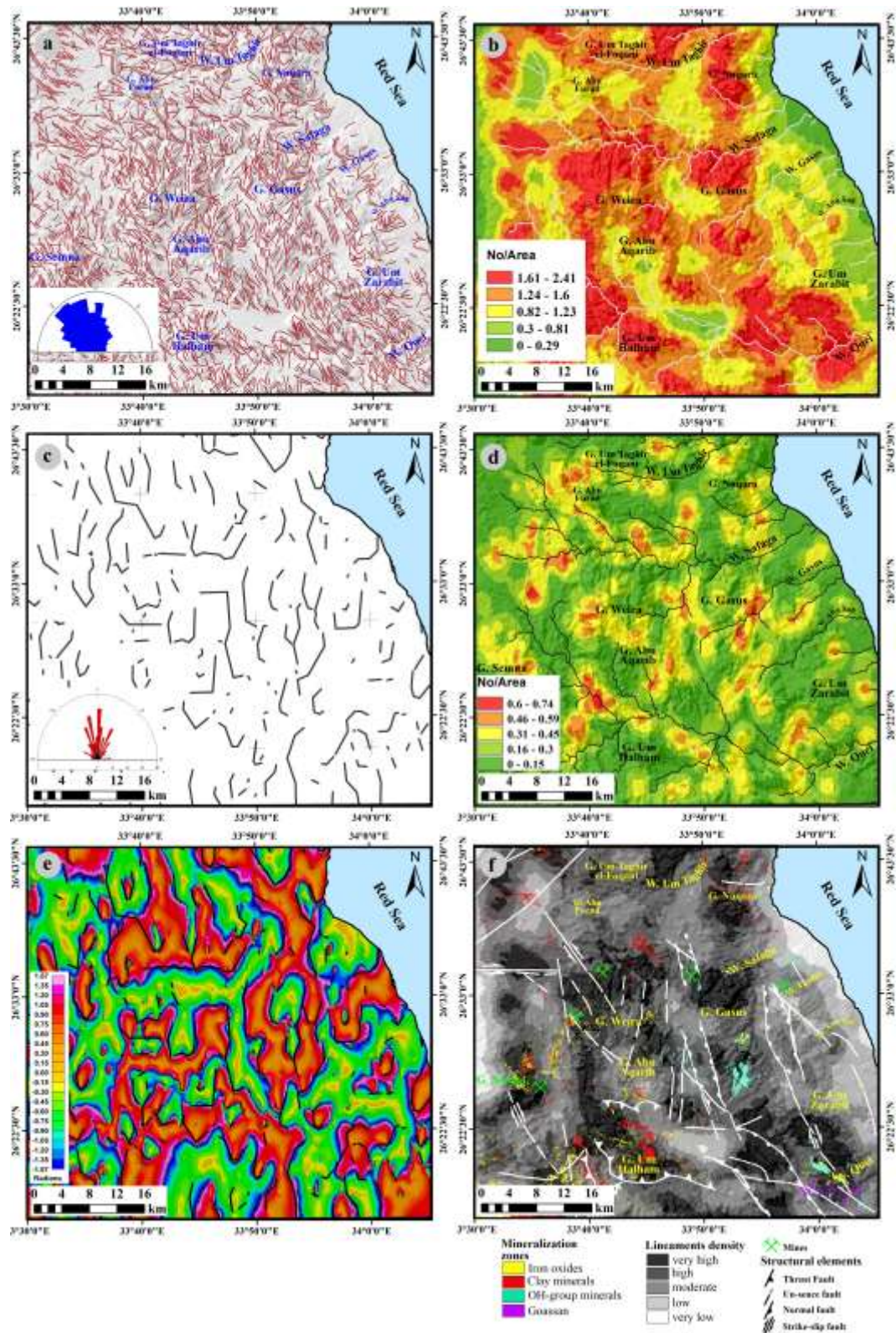


Fig. (5): (a) The lineaments map extracted from remotely sensed data (inset rose diagram), (b) The lineaments density map, (c) The vectorization map of the magnetic data showing linear structures (inset rose diagram), (d) The density map of vectorization, (e) The lineaments of the structural complexity superimposed on the edges of the source bodies of the horizontal tilt derivative and (f) The relation between the spatial distribution of the mineralized zones, lineaments and major structural elements.

REFERENCES

- Abd El-Wahed, M.; Zoheir, B.; Pour, A.B.; Kamh, S. (2021):** Shear-Related Gold Ores in the Wadi Hodein Shear Belt, South Eastern Desert of Egypt: Analysis of Remote Sensing, Field and Structural Data. *Minerals*, 11, 474. <https://doi.org/10.3390/min11050474>
- Abdelkareem, M., Akrby, A., Fakhry, M., and Mostafa, M., (2018a):** Using of remote sensing and aeromagnetic data for predicting potential areas of hydrothermal mineral deposits in the central east-ern desert of Egypt. *J. Rem. Sen.*, 7(1): 1-13.
- Abdelkareem, M., El-Din, G.M.K., and Osman, I., (2018b):** An integrated approach for mapping mineral resources in the Eastern Desert of Egypt. *Int. J. Appl. Earth Obser. Geo.*, 73: 682-696.
- Aero Service Company, (1984):** Final operational report of airborne Magnetic /radiation Survey in the Eastern Desert, Egypt. Aeroservice for EGPC, Houston, Texas, April 1984. Six volumes. *An internal report*. No. 3609.
- Ahmed, S.B., (2018):** Integration of airborne geophysical and satellite imagery data to delineate the radioactive zones at west Safaga Area, Eastern Desert, Egypt. *NRIAG J. Astr. Geo.*, 7(2): 297-308.
- Alexander, Io., Samuel, O.O., Esther, C.M., Theophilus, T.E., Kingsley, C.I., and Kingsley, C.N., (2015):** Integrating Landsat-ETM and Aeromagnetic data for enhanced structural interpretation over Naragwata area, North – Central Nigeria. *Int. J. Sci. Eng. Res.*, 6 (9): 2229-5518.
- Baranov, V., (1957):** A new method for interpretation of aeromagnetic maps: pseudogravimetric anomalies. *Geophys.*, 22: 359–383.
- Baranov, V., and Naudy, H., (1964):** Numerical calculation of the formula of reduction to the magnetic pole. *Geophy.*, 2: 67–79.
- Clark, R.N.; King, T.V.V.; Klejwa, M.; Swayze, G.A.; Vergo, N. (1990):** High spectral resolution reflectance spectroscopy of minerals. *J. Geophys. Res.* 95: 12653–12680.
- Cooper, G.R.J., and Cowan D.R., (2006):** Enhancing potential field data using filters based on the local phase. *Comput. Geo. Sci.*, 32: 1585–1591.
- Core, D., Buckingham, A., and Belfield, S., (2009):** Detailed structural analysis of magnetic data- done quickly and objectively, SGEF Newsletter.
- Egyptian Geological Survey and Mining Authority (EGSMA), (1992):** Geologic map of Al Qusayr Quadrangle, Scale, 1:250,000, *Geol. Surv.* Egypt, Cairo.
- El Gaby, S., List, F. K., and Tehrani, R., (1988):** Geology, evolution and metallogenesis of the Pan-African belt in Egypt. In S. El-Gaby, & R. O. Greiling (Eds.), *The Pan-African belt of northeast Africa and adjacent areas* (pp. 17–88). Wiesbaden: Vieweg-Verlag.
- Eldosouky, A.M., Sehsah, H., Elkhateeb, S.O., and Pour, A.B., (2020):** Integrating aeromagnetic data and Landsat-8 imagery for detection of post-accretionary shear zones controlling hydrothermal alter-ations: The Allaqi-Heiani Suture zone, South Eastern Desert, Egypt. *Adv. Space Res.*, 65(3): 1008-1024.

- Elkhateeb, S.O. and Abdellatif, M.A.G., (2018):** Delineation potential gold mineralization zones in a part of Central Eastern Desert, Egypt using Airborne Magnetic and Radiometric data. *NRIAG J. Astr. Geo.*, 7(2): 361-376.
- El-Magd, I.A., Mohy, H., and Basta, F., (2015):** Application of remote sensing for gold exploration in the Fawakhir area, Central Eastern Desert of Egypt. *Arab. J. Geosci.* 8 (6): 3523–3536.
- Fowler, A., and Osman, A.F., (2009):** The Sha'it–Nugrus shear zone separating Central and South Eastern Deserts, Egypt: a post-arc collision low-angle normal ductile shear zone. *J. Afr. Earth Sci.*, 53(1-2): 16-32.
- Gaafar, I.M., (2016):** Geophysical Surveys for defining favorable structures for Uranium remobilization in Wadi Yoider, Southern Eastern Desert, Egypt. *Egypt. Geophy. Soc., EGS J.* 14 (1): 149–164.
- Gabr, S., Ghulam, A., and Kusky, T., (2010):** Detecting areas of high-potential gold mineralization using ASTER data. *Ore Geology Rev.*, 38(1-2): 59-69.
- Gass, I.G., (1977):** The evolution of the Pan-African crystalline basement in NE Africa and Arabia. *J. Geol. Soc. London*, 134: 129–138.
- Greiling, P. O., Abdeen, M. M., Dardir, A. A., Akhal, E., El Ramly, M. F., Rashwan, A. A., and Sadek, M. F., (1994):** A structure synthesis of the Proterozoic Arabian-Nubian shield in Egypt. *Geologische Rundschau*, 83: 484–501.
- Grothaus, B., Eppler, D., and Ehrlich, R., (1979):** Depositional environment and structural implications of the Hammamat formation, Egypt. *Ann. Geol. Surv. Egypt*, IX, 564–590.
- Habib, M.E., (1987):** Arc-ophiolites in the Pan-African basement between Meatiq and Abu Furad, Eastern Desert, Egypt. *Bull. Fac. Sci. Assiut Univ.* 16 (1): 241–283.
- Holden, E.J., Dentith, M., and Kovesi, P., (2008):** Towards the automatic analysis of regional aeromagnetic data to identify regions prospective for gold deposits. *Comput. Geosci.* 34: 1505-1513.
- Holden, E.J., Kovesi, P., Dentith, M., Wedge, D., Wong, J.C., and Fu, S.C., (2010):** Detection of regions of structural complexity within aeromagnetic data using image analysis. In: *Twenty Fifth Int. Conf. of Image and Vis. Comp. New Zealand*.
- Hunt, G., (1977):** Spectral signatures of particulate minerals in the visible and near infrared. *Geophy.*, 42: 501–513.
- Ismail, A.A., (2008):** A study of the Effects of Various Regional Residual Separation Technique on Real Magnetic Data. *1st Arab Conf. on Astro. Geoph. Cairo, Egypt*
- Kadasi, A.N., (2015):** Interpretation of aeromagnetic data in terms of surface and subsurface geologic structures, southwestern Yemen: *Arab. J. Geo.*, 2: 1163–1179.
- Khamis, A.A. and Ayoub, R.R., (2014):** Features Controlling Radioelements Distribution in Al Aglab region, North Eastern Desert, Egypt. *Nuclear Sci. Sci. J.*, 3(1): 149-168.
- Kusky, T.M.; Ramadan, T.M. (2002):** Structural controls on Neoproterozoic mineralization in the South Eastern Desert, Egypt: An integrated field, Landsat TM, and SIR-C/X SAR

- approach *J. Afr. Earth Sci.*, 35: 107–121.
- Murphy, B.S., (2007):** Airborne geophysics and the Indian scenario. *J. Int. Geophys. Union*, 11 (1): 1–28.
- O'Conner, E. A., Bennett, J. D., Rashwan, A. A., Nasr, B. B., Mansour, M. M., Romani, R. F., and Sadek, M. F., (1993):** Crustal growth in the Nubian shield of south Eastern Desert, Egypt. *Proc. Inter. Conf. 30 Years Cooper.*, 189–195.
- Pour, A.B.; Park, T.S.; Park, Y.; Hong, J.K.; Zoheir, B.; Pradhan, B.; Ayoobi, I.; Hashim, M. (2018):** Application of multi-sensor satellite data for exploration of Zn-Pb sulfide mineralization in the Franklinian Basin, North Greenland. *Rem. Sens.*, 10: 1186.
- Sims, P. K., and James, H. L., (1984):** Banded iron-formations of late Proterozoic age in the central Eastern Desert, Egypt: Geology and tectonic setting. *Eco. Geol.*, 79: 1777–1784.
- Stern, R.J., (1985):** The Najd fault system, Saudi Arabia and Egypt: A late Precambrian rift-related transform system? *Tectonics*, 4: 497–511.
- Stern, R. J., and Hedge, C. E. (1985):** Geochronologic constraints on late Precambrian crustal evolution in the Eastern Desert of Egypt. *Am. J. Sc.*, 285(97–12).
- Stern, R. J., Gottfried, D., and Hedge, C. E., (1984):** Late Precambrian rifting and crustal evolution in the northeast Desert of Egypt. *Geo.*, 12: 168–172.
- Telford, W.M., Geldart, L.P., and Sheriff, R.E., (1990):** Applied Geophysics, 2nd ed. Cambridge University Press.
- Windley, B. F., (1996):** The evolving continents. *Oceanographic Liter. Rev.*, 8(43): p.785.
- Xiong, S.Q., Ding, Y.Y., and Li, Z.K., (2014):** Characteristics of China Continental magnetic basement depth: *Chinese. J. Geophys.*, 57 (12): 3981–3993.
- Zaki, O.A., AbdAlnabi, S.H., Abd El Wahab, S.E., Ismail, A.A. and Soliman, N.M., (2017):** Aeromagnetic signature analysis of Gasus area and its surrounding, central eastern desert, Egypt. *Arab. J. Geosci.*, 10(14): 1-20.
- Zoheir, B.; Emam, A.; Abdel-Wahed, M.; Soliman, N. (2019):** Multispectral and Radar Data for the Setting of Gold Mineralization in the South Eastern Desert, Egypt. *Rem. Sens.*, 11: 1450.
- Scull, P., Franklin, J., Chadwick, O.A., and McArthur, D. (2003):** Predictive soil mapping: A review. *Progr. Phys. Geogr.*, 27: 171–197 .
- Van Houten, F. B., Bhattacharyya, D. P., and Mansour, S. El., (1984):** Cretaceous Nubia formation and correlative deposits, eastern Egypt: Major regressive-transgressive complex. *Geol. Soc. Am. Bull.*, 95: 397-405.
- Zaghloul, Z. M., (1983):** On the discovery of Paleozoic trace fossils Bifungites, in the Nubian sandstone facies of Aswan, Egypt, *J. Geol.*, 27(1-3): 65-72.

تكمال بيانات الاستشعار عن بعد والمغناطيسية الجوية لاستخراج العناصر التركيبية ونطاقات التمعينات في منطقة سفاجا، الصحراء الشرقية، مصر

حامد الرفاعي^١ وسمير زكي قمح^٢ ومحمد الحسيني^١

^١ قسم الجيولوجيا – كلية العلوم – جامعة كفر الشيخ – مصر
^٢ قسم الجيولوجيا – كلية العلوم – جامعة طنطا – مصر

تعتبر عملية تحديد والتعرف على العناصر التركيبية والتمعنات المصاحبة لها من الخطوات الأساسية في عمليات الاستكشاف المعدني واستخراج موارد معدنية جديدة تساعد في الأغراض الصناعية والدخل القومي. لذلك يعتبر الهدف الرئيسي لهذه الدراسة هو استخراج العناصر التركيبية ونطاقات التمعينات المصاحبة وكذلك النطاقات الواعدة لعمليات التعدين. لذا تعتبر عملية تكامل بيانات الاستشعار عن بعد والمغناطيسية الجوية من النهج المتقدمة في تحديد العناصر التركيبية والتمعنات المصاحبة. فقد تم استخدام مرئيات فضائية من نوع لاندسات-٨ وسنتينل-٢ لعملية التعرف وفصل الصخور المختلفة وإنتاج خريطة جيولوجية محدثة لمنطقة الدراسة. كما تم استخدام البيانات الرادارية للقمر سنتينل-١ لاستنباط العناصر التركيبية الخطية والتي أظهرت عدد كبير منها وقد اتخذت الاتجاهات التركيبية التالية: شمال غرب-جنوب شرق و شمال شمال غرب – جنوب جنوب شرق و شمال-جنوب و شمال شرق – جنوب غرب. بالإضافة الى بيانات الاستشعار فقد استخدمت بيانات المغناطيسية الجوية المعالجة وقد أوضحت بوجود شواذ للمغناطيسية المتبقية وتم تحديد الحواف الخطية. كما تم تحديد العناصر التركيبية التحت سطحية ومعرفة اتجاهاتها من خلال تفسير بيانات اويلر. وقد أوضحت النتائج بوجود توافق بين اتجاهات العناصر الخطية المستنتجة من الاستشعار عن بعد والمغناطيسية الجوية والتكامل بين هذه النتائج اظهر بوجود دور كبير للعناصر التركيبية في توجدات النطاقات التعدينية.